Atomic-number (*Z*)-correlated atomic sizes for deciphering electron microscopic molecular images

Junfei Xing[a] [iD], Keishi Takeuchi[a], Ko Kamei[a], Takayuki Nakamuro[a] [iD], Koji Harano[a,1], and Eiichi Nakamura[a,1]

With the advent of atomic resolution transmission electron microscopy (AR-TEM) achieving sub-Ångstrom image resolution and submillisecond time resolution, an era of cinematic molecular science where chemists can visually study the time evolution of molecular motions and reactions at atomistic precision has arrived. However, the appearance of experimental TEM images often differs greatly from that of conventional molecular models, and the images are difficult to decipher unless we know in advance the structure of the specimen molecules. The difference arises from the fundamental design of the molecular models that represent atomic connectivity and/or the electronic properties of molecules rather than the nuclear charge of atoms and electrostatic potentials that are felt by the e-beam in TEM imaging. We found a good correlation between the atomic number (*Z*) and the atomic size seen in TEM images when we consider shot noise in digital images. We propose *Z*-correlated (ZC) atomic radii for modeling AR-TEM images of single molecules and ultrathin crystals with which we can develop a good estimate of the molecular structure from the TEM image much more easily than with conventional molecular models. Two parameter sets were developed for TEM images recorded under high-noise (ZC$_{HN}$) and low-noise (ZC$_{LN}$) conditions. The molecular models will stimulate the imaginations of chemists planning to use AR-TEM for their research.

atomic radius | molecular model | structural analysis | single-molecule imaging | transmission electron microscopy

The world of atoms and molecules invisible to human eyes has been illuminated by the development of three-dimensional models in which atoms represented by spheres are connected to each other with appropriate spatial disposition. Here, the choice of the radii of the spheres, in addition to coloring, is the most crucial visual identifier of atoms and atomic ions, and a variety of useful constructions of radii, either empirical or quantum mechanical (1, 2), have been proposed in accord with chemical intuition. Whereas wire and ball-and-stick models are primitive, showing only bond lengths, bond angles, and torsional angles, chemists have implemented further information into molecular models. Representing the van der Waals isosurface, a Corey–Pauling–Koltun (CPK) model was developed to illustrate the molecular surface for analysis of intermolecular interactions (3). Shannon's ionic model (4) is useful for inorganic chemistry. The atomic radii chosen in these models reflect the electronic properties of atoms and molecules.

With the advent of atomic-resolution transmission electron microscopy (AR-TEM) achieving sub-Ångstrom image resolution and submillisecond time resolution (5–8), an era of "cinematic molecular science" has arrived, where chemists can visually study the time evolution of molecular motions and reactions at atomistic precision (9–11). However, experimental TEM images often differ greatly from what chemists expect using their favorite molecular models (Fig. 1), and this discrepancy contributed to reducing the popularity of AR-TEM in molecular science. The difficulty is particularly important when we deal with unknown structures that are mobile and lack structural periodicity. For example, structure assignment of the AR-TEM images of a rotating zinc cluster (Fig. 1*A*) that forms in the synthesis of a crystal of a metal–organic framework (MOF; MOF-5) (12) was impossible without reducing the number of initial guess structures down to several hundred from a total of 4,096 isomers and their rotamers as to the 2-iodo-1,4-phenylene bridges (Fig. 1 *D* and *E*). Here, we found the CPK atomic radii (Fig. 1*B*) more confusing than revealing, and we became convinced of a need for new atomic radii that better represent the experimental images (compare Fig. 1 *B* and *C*). In doing so, we found that the atom size seen in TEM images shows a strong correlation to the atomic number (*Z*), particularly if we consider the shot noise in digital images. In a noise-free image, we find little correlation, as theory predicts (13). Our idea may be symbolically described as comparing

Significance

Atomic resolution transmission electron microscopy (TEM) has opened up a new era of molecular science by providing atomic video images of dynamic motions of single organic and inorganic molecules. However, the images often look different from the images of molecular models, because these models are designed to visualize the electronic properties of the molecule instead of nuclear electrostatic potentials that are felt by the e-beam in TEM imaging. Here, we propose a molecular model that reproduces TEM images using atomic radii correlated to atomic number (*Z*). The model serves to provide a priori a useful idea of how a single molecule, molecular assemblies, and thin crystals of organic or inorganic materials look in TEM.
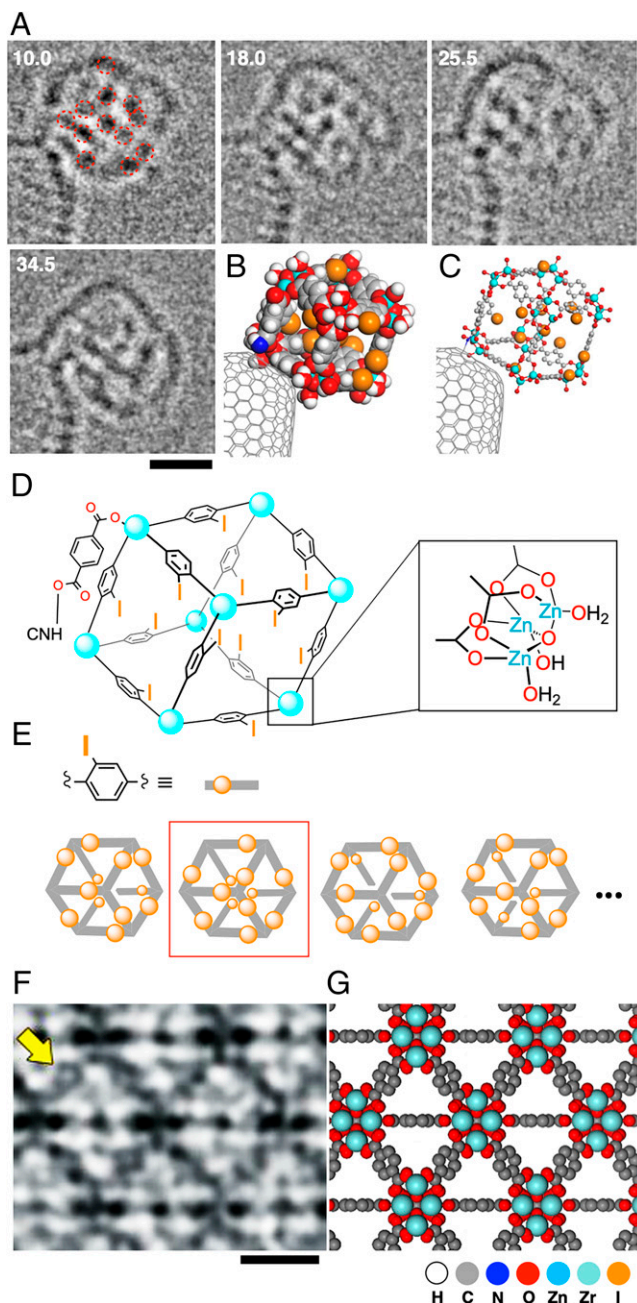
Fig. 1. Experimental AR-TEM image and atomic-number-correlated molecular model (ZC model). (*A*) Time evolution of TEM image of a MOF-5 precursor, a cubic cluster made of Zn^{2+} and 2-iodoterephthalic acid captured on a carbon nanotube. The molecular images are blurred by rotation and vibration. Time is shown in seconds. Taken from ref. 12 (Copyright 2019, Nature Publishing Group). (*B*) A CPK model corresponding to the image at 10.0 s. (*C*) A ZC_{HN} model also for the image at 10.0 s. (*D*) Chemical structure of the cubic cluster. (*E*) Schematic illustration of isomers of the cubic MOF-5 precursor. Four structures out of 4096 possible isomers are shown. The structure seen in Fig. 1*A* is highlighted by a red square. (*F*) TEM image of an ultrathin crystal of UiO-66 (adapted from ref. 15). The benzene ring in a benzene dicarboxylate linker is indicated by an arrow (Copyright 2018, The American Association for the Advancement of Science). (*G*) A ZC_{LN} model corresponding to (*F*). (Scale bars: 1 nm.)

the sizes of mountains by measuring the width of the lowest portion of each mountain that is visible above a sea of clouds. We report here a set of *Z*-correlated (ZC) atomic radii for deciphering AR-TEM images, with which we can develop a good estimate of the molecular structure from the TEM image much more easily than with conventional molecular models. Two parameter sets are described: one for TEM images under high-noise conditions

(ZC_{HN}, Fig. 2*C*) and another under low-noise conditions (ZC_{LN}, Fig. 2*D*). The former is useful for single-molecule imaging and the latter for an ultrathin film such as UiO-66 MOF (Fig. 1*F*) (14, 15). The ZC radii reflect the relative sizes of various elements and help chemists develop an initial estimate of the molecular structures. Note, however, that we do not intend the ZC model to reproduce the TEM images exactly. No chemists expect the CPK model to represent the van der Waals properties of the molecule exactly, and molecular models are there to stimulate chemists' imaginations.

In Fig. 2, we compare the atomic radii used in the CPK model, Shannon's ionic model, and the ZC_{LN} and ZC_{HN} models. CPK radii are smaller for transition metals and larger for main group elements, and Shannon's radii decrease with the increasing atomic number within the same period. These atomic radii are unsuitable for deciphering AR-TEM images, where the behavior of the e-beam in the electrostatic potential created by atomic nuclei plays a decisive role (16, 17). In the ZC model proposed here, the atomic radius shows element dependence, changing systematically as *Z* increases. The ZC_{HN} atomic radii (Fig. 2*C*) are smaller in signal size than the ZC_{LN} radii (Fig. 2*D*), show large *Z*-dependence, and are suitable for fast molecular imaging where the level of shot noise is large (Fig. 1 *A*–*C*) (18). The ZC_{LN} radii are suitable for images of ultrathin crystalline films where the level of shot noise is comparatively low. The atomic sizes for the graphical construction of the ZC models are listed in Fig. 2*E*. We anticipate that the molecular model will stimulate the imaginations of chemists planning to use AR-TEM for their research.

Results and Discussion

Experimental study of individual molecules at an atomistic level has been a challenge for chemists. Scanning probe microscopy is largely limited to imaging static specimen molecules on a flat substrate (19, 20). Utilizing specimens attached to a substrate or those comprising a part of a large crystal, the conventional TEM technique has suffered from similar limitations. AR-TEM imaging of single molecules in or on a carbon nanotube (CNT) (10) or on graphene (21, 22) has realized dynamic molecular imaging against a vacuum background, hence opening an avenue to single-molecule atomic-resolution time-resolved electron microscopic (SMART-EM) imaging (23). Here, we can study the time evolution of structural changes and reactions with up to millisecond speed and sub-Å spatial resolution (18). The method produces a series of two-dimensional projection images where information on three-dimensional locations and properties of atomic nuclei is hidden (Fig. 1*A*). Here, we see several dense and large signals, and less dense and smaller signals, ascribable to iodine and light atoms, respectively. As applied to a MOF named UiO-66, TEM provided an image depicting the zirconium atom as both dense and very large spots, and benzene rings as faint and small signals (yellow arrow, Fig. 1*F*). We felt that this density/size correlation found in these TEM images does not match the theory because the signal size should be independent of *Z* (13), while the signal intensity of individual atoms should depend on *Z* (16, 24), empirically, $Z^{2/3}$ (25, 26). In the present study, we found that the signal size does show significant *Z*-dependence if we take into account the shot noise present in every TEM image (27). We exploited this dependence in defining the atom radii for the ZC model.

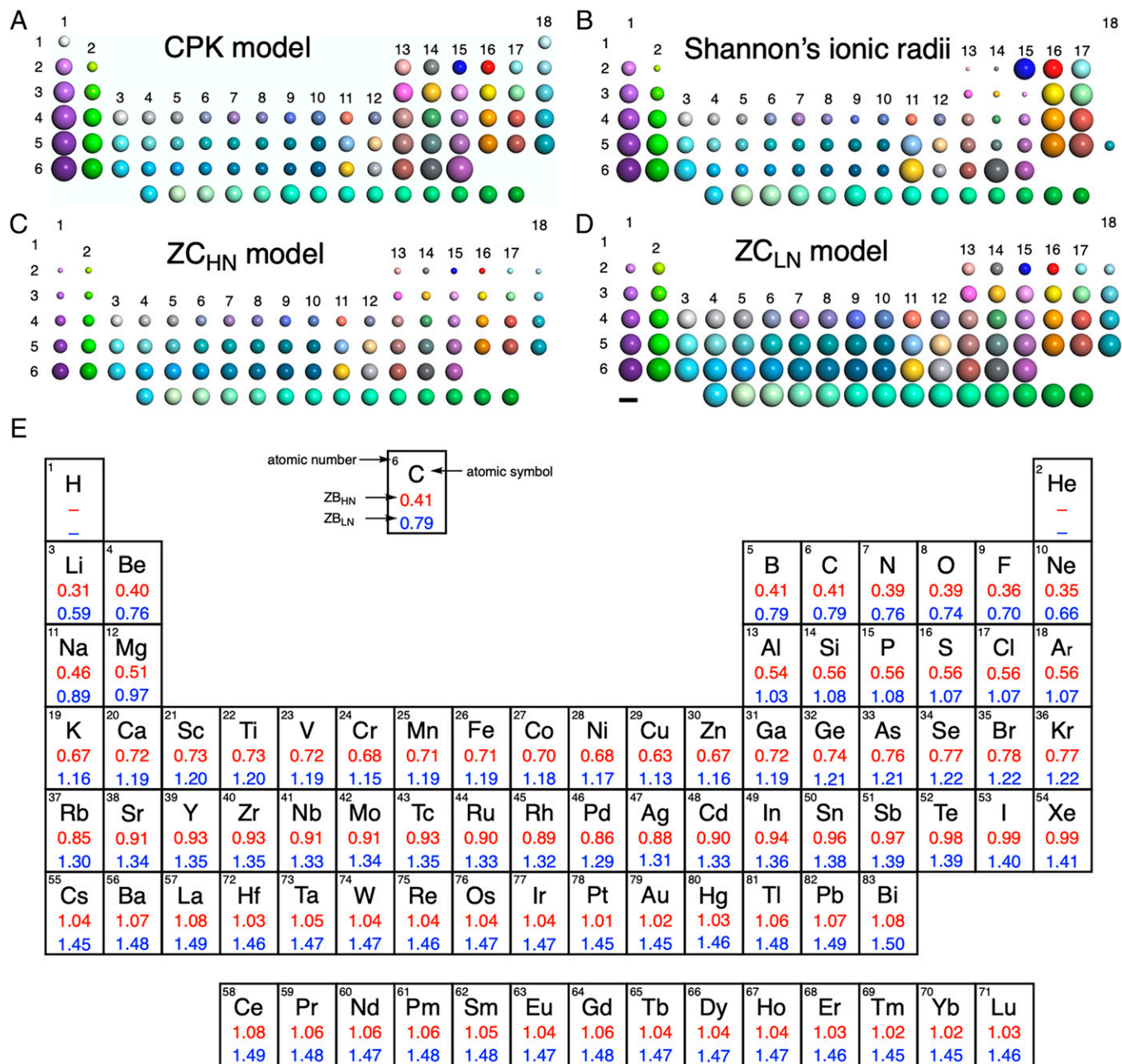For molecules and molecularly thin objects, TEM images largely comprise the phase contrast created by interference

Fig. 2. Periodic table of atomic sizes used in molecular models. (*A*) CPK model. (*B*) Shannon's ionic parameters. (*C*) ZC_{HN} model. (*D*) ZC_{LN} model. (Scale bar: 2 Å.) (*E*) List of ZC_{HN} radii for single-molecule imaging and ZC_{LN} radii for ultrathin crystals (in Å).

(*E*) Each element box lists: atomic number, atomic symbol, ZB_{HN} (red), ZB_{LN} (blue).

Z	El	ZB_{HN}	ZB_{LN}
1	H	—	—
2	He	—	—
3	Li	0.31	0.59
4	Be	0.40	0.76
5	B	0.41	0.79
6	C	0.41	0.79
7	N	0.39	0.76
8	O	0.39	0.74
9	F	0.36	0.70
10	Ne	0.35	0.66
11	Na	0.46	0.89
12	Mg	0.51	0.97
13	Al	0.54	1.03
14	Si	0.56	1.08
15	P	0.56	1.08
16	S	0.56	1.07
17	Cl	0.56	1.07
18	Ar	0.56	1.07
19	K	0.67	1.16
20	Ca	0.72	1.19
21	Sc	0.73	1.20
22	Ti	0.73	1.20
23	V	0.72	1.19
24	Cr	0.68	1.15
25	Mn	0.71	1.19
26	Fe	0.71	1.19
27	Co	0.70	1.18
28	Ni	0.68	1.17
29	Cu	0.63	1.13
30	Zn	0.67	1.16
31	Ga	0.72	1.19
32	Ge	0.74	1.21
33	As	0.76	1.21
34	Se	0.77	1.22
35	Br	0.78	1.22
36	Kr	0.77	1.22
37	Rb	0.85	1.30
38	Sr	0.91	1.34
39	Y	0.93	1.35
40	Zr	0.93	1.35
41	Nb	0.91	1.33
42	Mo	0.91	1.34
43	Tc	0.93	1.35
44	Ru	0.90	1.33
45	Rh	0.89	1.32
46	Pd	0.86	1.29
47	Ag	0.88	1.31
48	Cd	0.90	1.33
49	In	0.94	1.36
50	Sn	0.96	1.38
51	Sb	0.97	1.39
52	Te	0.98	1.39
53	I	0.99	1.40
54	Xe	0.99	1.41
55	Cs	1.04	1.45
56	Ba	1.07	1.48
57	La	1.08	1.49
72	Hf	1.03	1.46
73	Ta	1.05	1.47
74	W	1.04	1.47
75	Re	1.04	1.46
76	Os	1.04	1.47
77	Ir	1.04	1.47
78	Pt	1.01	1.45
79	Au	1.02	1.45
80	Hg	1.03	1.46
81	Tl	1.06	1.48
82	Pb	1.07	1.49
83	Bi	1.08	1.50
58	Ce	1.08	1.49
59	Pr	1.06	1.48
60	Nd	1.06	1.47
61	Pm	1.06	1.48
62	Sm	1.05	1.48
63	Eu	1.04	1.47
64	Gd	1.06	1.48
65	Tb	1.04	1.47
66	Dy	1.04	1.47
67	Ho	1.04	1.47
68	Er	1.03	1.46
69	Tm	1.02	1.45
70	Yb	1.02	1.45
71	Lu	1.03	1.46

between the transmitted wave and the wave scattered by the atoms (16). The signal intensity $g(x)$ is determined by the following equation (25):

$$g(\boldsymbol{x}) = \mid 1 + 2\pi i \int_0^{k_{max}} f_e(k)\exp\left[-i\chi(k)\right]J_0(2\pi kr)kdk \mid^2,$$

where $f_e(k)$ is the electron scattering factor, $\chi(k)$ is the aberration function, k_{max} is the maximum spatial frequency in the objective aperture, and $J_0(x)$ is the Bessel function of order zero. Among these parameters, only $f_e(k)$ is dependent on Z. The electron scattering factor $f_e(q)$ is calculated from the X-ray scattering factor $f_x(q)$ and Z based on the Mott-Bethe equation (25):

$$f_e(q) = \frac{1}{2\pi^2 a_0}\left(\frac{Z - f_X(q)}{q^2}\right),$$

where q is the magnitude of the three-dimensional wavevector that is the difference between the incident and scattered X-ray,

and a_0 is the Bohr radius. In principle, the electron scattering factor is proportional to the power of Z, but it is smaller than the first power due to the term of the X-ray scattering factor $f_X(q)$. The proportionality of the signal intensity to $Z^{2/3}$ is approximated from the fitting of the plot of intensity-Z dependence (25). These scattering factors can be obtained from quantum mechanical calculations, but for current TEM simulations, in order to reduce the computational cost, we use a parameterized electron scattering factor described by a combination of Lorentzian and Gaussian factors proposed by Weickenmeier and Kohl (28) and it is also adopted in this study.

We generated theoretically simulated TEM images using the multislice simulation software ElBis incorporating a shot noise calculation algorithm developed by Hosokawa (29). We studied commonly encountered elements between $Z = 1$ and 83 with defocus value (df) = −10 nm and acceleration voltage of 80 kV, which are the conditions typical for imaging molecules and
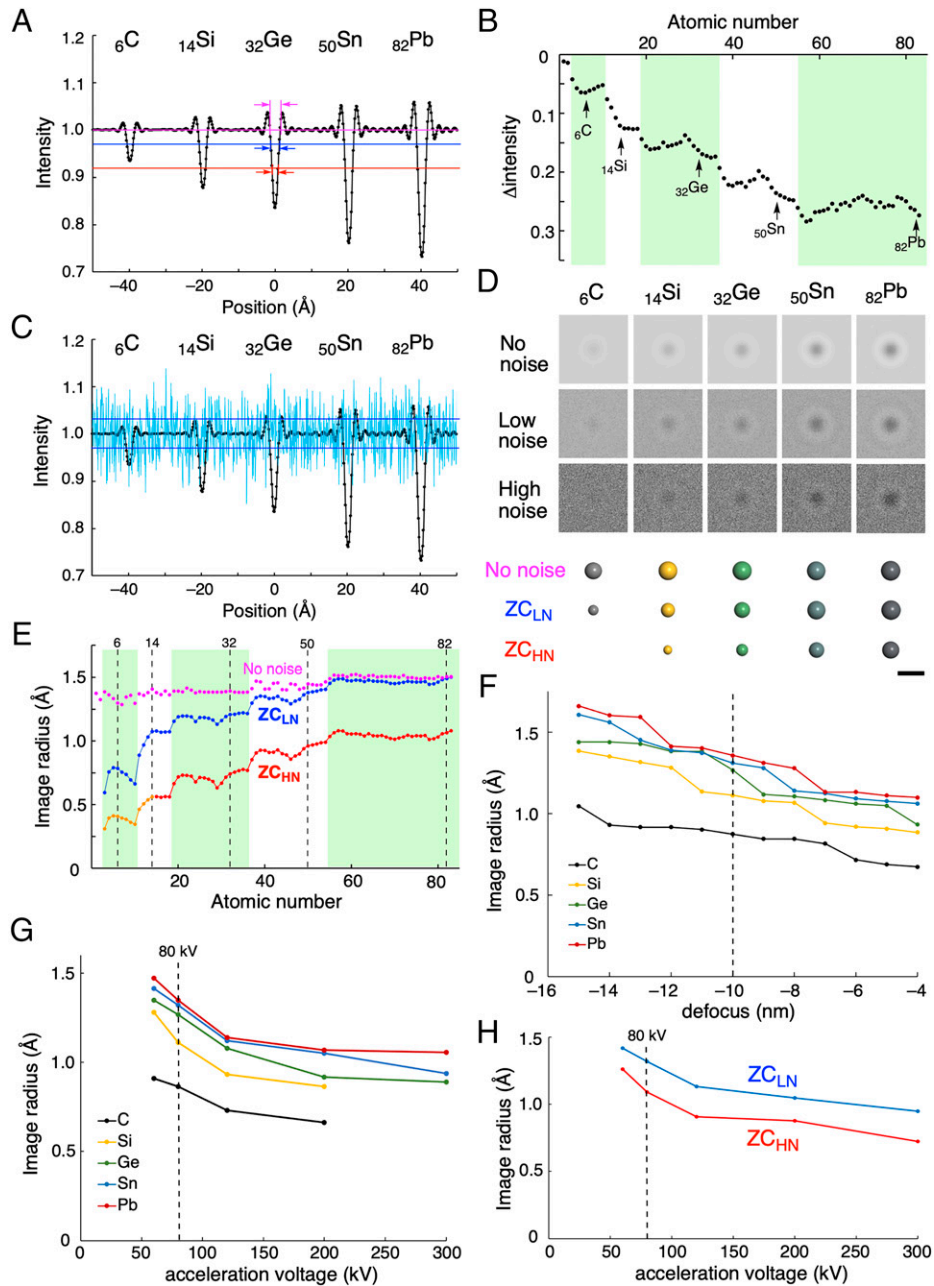
Fig. 3. Image size of a single atom in simulated TEM images (80 kV, defocus = −10 nm). (*A*) Intensity profile of simulated images without noise of carbon, silicon, germanium, tin, and lead atoms (i.e., images taken at an infinitely large e-dose). The intensity is normalized to the background intensity as 1 (purple line). Blue and red lines show a noise level corresponding to 4.5×10^6 e$^-$ nm^{-2} frame^{-1} (LN condition, maximum e-dose available in the software), and 5.0×10^5 e$^-$ nm^{-2} frame^{-1} (HN condition), respectively. (*B*) Intensity difference between a peak top and the background for a single atom. Periods 2, 4, and 6 are highlighted by light green. (*C*) Intensity profile of the single-atom images shown together with low-level shot noise (shown as light blue). The noise level is shown as SD (blue line as in *A*). (*D*) Simulated images under no-noise, LN, and HN conditions. Corresponding atom models. (Scale bar: 5 Å.) (*E*) *Z*-dependence of the no-noise (purple), ZC_{HN} (blue), and ZC_{LN} (red) atomic radii. For atoms smaller than $Z = 14$ (orange line), we scale down the ZC_{LN} sizes because the images are so faint that we could not determine the signal size. The TEM simulation software EIBis outputs the data as pixel images, and hence the data are noncontinuous. (*F*) Defocus-dependence of ZC_{LN} image radii shown for group 14 elements. (*G*) Acceleration voltage dependence of ZC_{LN} image radii for group 14 elements. Carbon and silicon atoms are invisible at 300 kV. (*H*) Acceleration voltage dependence of ZC_{LN} (blue) and ZC_{HN} (red) image radii for iodine ($Z = 53$).

their assemblies (30–34). The atomic radii in the ZC_{LN} and ZC_{HN} models are defined as described in the following paragraphs.

In Fig. 3*A*, we show the phase contrast without shot noise for group 14 elements placed 20 Å away from each other. The intensity profile consists of a triangular peak flanked by a series of fringe signals and the height of the triangle increases as Z increases, roughly proportional to $Z^{2/3}$ (Fig. 3*B*, see *SI Appendix,* Fig. S1 for simulation images of all the elements) (25, 26). The small undulation of the signal height for each period reflects the Z-dependence of nuclear charge (13).

The base of the isosceles triangle, on the other hand, shows little Z-dependence (purple arrows, Fig. 3*A*) as reported previously (13), which led us to contemplate the origin of the experimentally observed Z-dependence of the image sizes. Some trial-and-error studies revealed that the length of the bottom of the triangle shows Z-dependence when the triangle is truncated by background noise. An intensity profile of the single-atom images overlaid with a background noise corresponding to an electron dose (e-dose) of 4.5×10^6 e$^-$ nm^{-2} frame^{-1} is shown in Fig. 3*C*, where we see an obvious effect of noise on the apparent signal height and also on the apparent radius of

the signal, the noise acting like the sea of clouds that truncates the view of mountains. Thus, we set the SD of the background noise as the threshold for visual recognition (35). Cutting the triangle of the noise-free atom signals at low and high noise levels (LN and HN, blue and red lines in Fig. 3A) produces smaller isosceles triangles, and we use the length of the bottom of these triangles (image radius in Fig. 3E) as the atomic radii of the ZC_{LN} and ZC_{HN} models shown in Fig. 2E. The blue line represents the LN conditions of an e-dose of 4.5×10^6 e$^-$ nm^{-2} frame^{-1} and the red line the HN conditions of an e-dose of 5.0×10^5 e$^-$ nm^{-2} frame^{-1}—a typical dose used for fast molecular imaging using a complementary metal oxide semiconductor (CMOS) detector (12). In Fig. 3D, we illustrate simulations of atomic images without shot noise and with low and high noise, to which the ZC_{HN} and ZC_{LN} models compare favorably (see *SI Appendix*, Figs. S2 and S3 for simulated images under LN and HN conditions for all the elements).

In Fig. 3E, we summarize graphically the image radii calculated by truncating the bottom of the atomic signal with three noise threshold values (no, low, and high noise level) for all elements for $Z = 1$–83. A small undulation due to variation of effective nuclear charge (Z_{eff}) is also seen, and the atom image size of the atoms increases while the Z_{eff} drops significantly at the point where the period changes. This is because the electron cloud of an atom spread more to the outer side at high-period elements. Numerical data on the ZC atomic radii are summarized in Fig. 2E and the atomic images are summarized in Fig. 2 C and D. In our previous report (12), we empirically found a correlation between Z and apparent atomic radii, and here we propose the ZC model on a solid and broad basis. Although the variation of df (–4 to –15 nm, Fig. 3F) systematically changes the image radii by less than 20%, the trend of element dependence of the radius still holds (36). The element dependence remains to be seen under the different acceleration voltages ranging from 60 to 300 kV (Fig. 3G), and under both LN and HN conditions (Fig. 3H). Although TEM images may be blurred for various reasons such as specimen motions, energy spread of the e-beam, defocus, and pixel, they contribute equally to all elements and hence does not much affect the Z-dependence of the image radii. Technical improvement will reduce the magnitude of blurring in the near future.

Signal height and the signal radius truncated by shot noise level increase as several atoms are overlapped along the axis of an e-beam (37). Fig. 4A shows the intensity profile of simulated images of five hypothetical cumulene molecules placed along the e-beam, whereas Fig. 4 B–D shows the simulated images under no-noise, LN, and HN conditions, respectively. As we impose a shot noise of 5.0×10^5 e$^-$ nm^{-2} frame^{-1} (red line, corresponding to the HN condition), single C and C–C placed perpendicular to the e-beam become hidden behind the noise, while larger molecules remain to be seen above the background noise (Fig. 4D) (38). The image size of the overlapped carbon atoms in the HN image (Fig. 4D second *Left*) becomes comparable with the single atom image in the LN image (Fig. 4C most *Left*). A similar effect of atom overlap is observed also for nitrogen and oxygen. In Fig. 1A, we see the effect of overlapping carbon and oxygen atoms in the outline of the zinc cluster molecule.

In Fig. 5, we show several applications of the ZC model to SMART-EM imaging of organic and metallic molecular entities, where we use the ZC_{HN} parameters and CPK model as a reference. Images in Fig. 5 A and C were taken on an instrument without aberration correction with a CCD camera at 120 kV, the one in Fig. 5E on an aberration-corrected TEM with a CCD
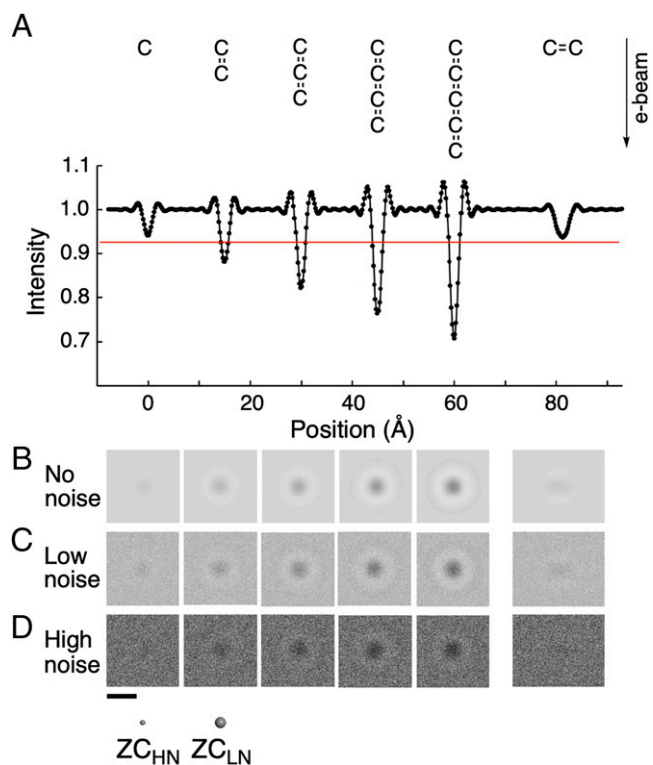

Fig. 4. Simulated TEM images of overlapping carbon atoms. (A) Intensity profile of hypothetical cumulene molecules. The red line shows a noise level corresponding to an e-dose of 5.0×10^5 e$^-$ nm^{-2} frame^{-1} (high noise threshold in Fig. 3). (B) Simulated TEM images under the no-noise condition. (C) Simulated images under the LN condition. (D) Simulated images under the HN condition. Atom sizes of carbon for ZC_{HN} and ZC_{LN} models are also shown. (Scale bar: 5 Å.)

camera at 120 kV, and those in Fig. 5 B, D, F, and G on an aberration-corrected TEM equipped with a CMOS camera at 80 kV. In all cases, the ZC_{HN} model that has been designed to represent atomic nuclei looks much closer to the TEM image than the space-filling model that represents the molecular surface (*SI Appendix*, Fig. S4 for visual comparison).

Fig. 5A illustrates a fullerene molecule bearing a perfluoroalkyl chain (39). The fullerene moiety is elliptical because of vibration of the molecule along the CNT axis during imaging (0.5 s frame^{-1}). Fig. 5B shows α-cyclodextrin (α-CD), a cyclic hexamer of glucose, sliding near the apex of a carbon nanohorn (CNH) (7). The ZC model matches the TEM image better than the CPK model. The larger size of individual dark spots in the TEM image than the ZC atoms is due to blurring caused by motions of the α-CD molecule during the 0.5 s exposure time (7). Fig. 5C shows a TEM image (0.5 s frame^{-1}) of a structurally mobile van der Waals complex involving 1,3,5-Tris(4-bromophenyl)benzene (40), and the mobility is supported by the broad TEM image (blurring) as compared with the more compact image of the ZC model. The location of eight bromine atoms can be more easily identified by the ZC model than by the CPK model. Fig. 5D illustrates a trinuclear molybdenum complex attached to a hole on the graphitic surface of a CNH (41). The crucial three molybdenum atoms are visible in the ZC model, while they are hidden behind oxygen atoms in the CPK model. Fig. 5E shows an example of a TEM image of thyroxine, an amino acid containing four iodine atoms. The molecule interacts with the ammonium ion moiety on the tip of a CNT at 6.0 s and slides gradually downward during 54.0 s, accompanying conformational change around the flexible ether linkage.
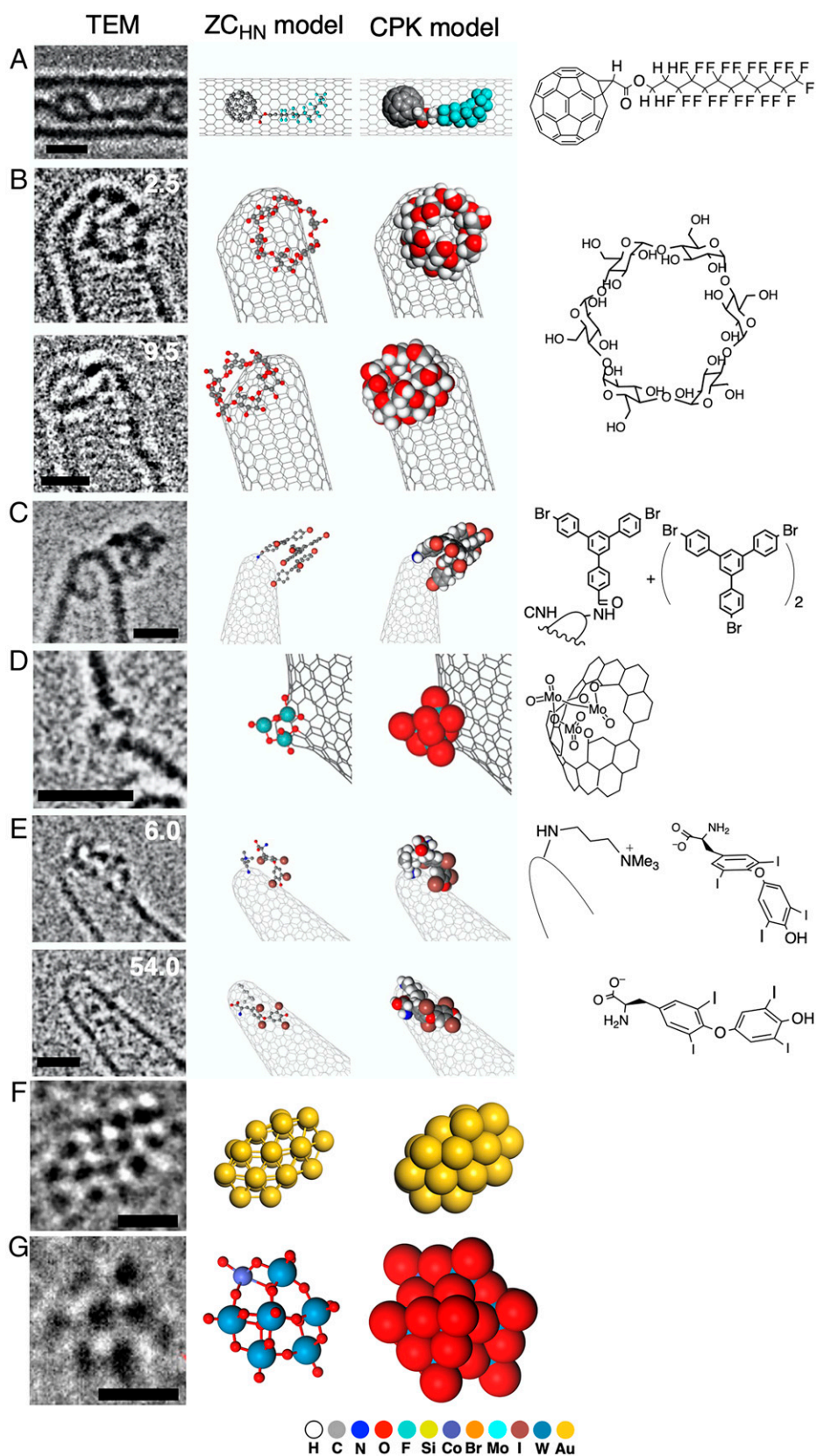
Fig. 5. Experimental AR-TEM image and ZC_{HN} model. (*A*) Perfluoroalkyl [60]fullerene in a single-walled CNT. See *SI Appendix,* Fig. S4 for a comparison of the TEM image and the ZC_{HN} model image (Copyright 2014, American Chemical Society). (*B*) Time evolution of TEM image of α-CD sliding on the CNH (Copyright 2021, American Chemical Society). (*C*) A termolecular van der Waals cluster on the CNH (Copyright 2012, Nature Publishing Group). (*D*) A trimolybdenum oxo cluster formed at an oxidized defect of the CNH (Copyright 2021, Chemical Society of Japan). (*E*) Time evolution of the TEM image of a thyroxine molecule changing its conformation and orientation on a CNH bearing a trimethylammonium ion linker. (*F*) A Au_{24} cluster on an amorphous carbon film (Copyright 2021, American Chemical Society). (*G*) A $[CoSiW_{11}O_{39}]^{6-}$ cluster on graphene oxide. The silicon atom is hidden behind a tungsten atom (Copyright 2016, American Chemical Society). (Scale bars: 1 nm for *A*–*E* and 0.5 nm for *F* and *G*.)
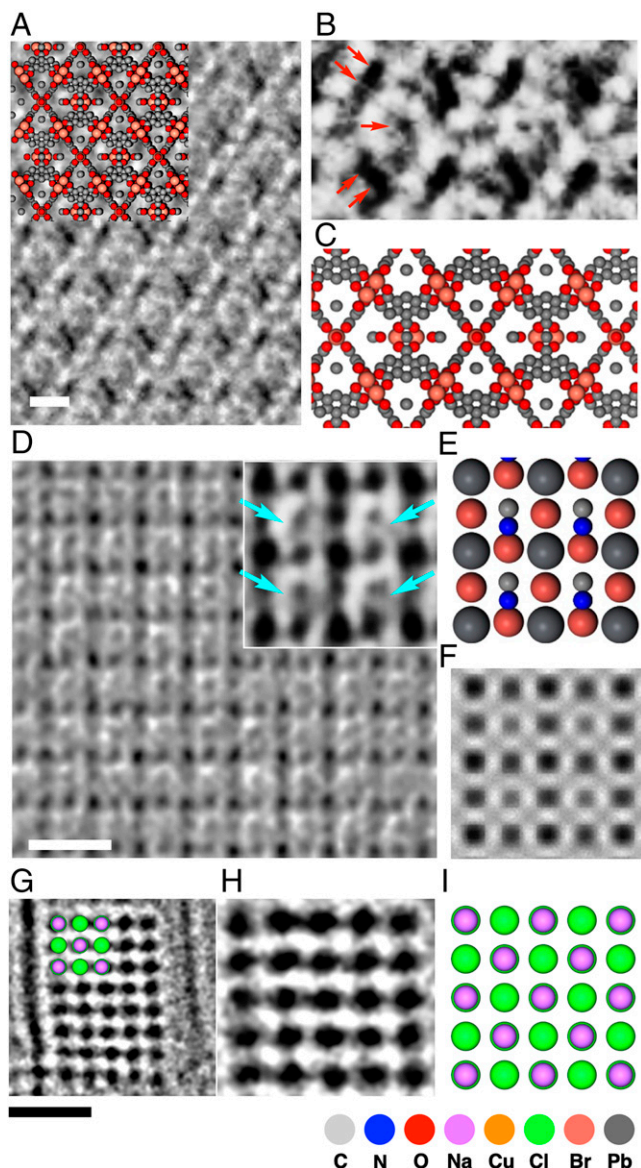
Fig. 6. Experimental TEM image and ZC_{LN} model for thin crystals of organic–inorganic hybrid materials and an ionic salt. (*A*) TEM image of HKUST-1 (Copyright 2018, The American Association for the Advancement of Science). (*B*) A magnified view of *A*. Arrows indicate overlapped Cu atoms. (*C*) ZC_{LN} model corresponding to *B*, which is also shown in the *Upper Left* corner in *A*. (*D*) TEM image of MAPbBr₃ and a magnified view (*Inset*). Arrows indicate MA ions (Copyright 2018, The American Association for the Advancement of Science). (*E*) ZC_{LN} model corresponding to *D*. (*F*) TEM simulation corresponding to *E* under the LN condition. (*G*) TEM image of a nanocrystal of NaCl in CNT (Copyright 2021, American Chemical Society). (*H*) A magnified view of *G*. (*I*) ZC_{LN} model corresponding to *H*, which is also shown in the *Upper Left* of *G*. (Scale bars: 1 nm.)

The advantage of the ZC model over conventional models such as wire, ball-and-stick, and CPK models is best illustrated with transition metal clusters. Fig. 5*F* shows a TEM image of a Au₂₄ cluster on amorphous carbon, where the locations of the metal atoms are clearly discernable (42). In an image of a $[CoSiW_{11}O_{39}]^{6-}$ polyoxometalate cluster in Fig. 5*G* (43), we find only Co and W metal atoms. Accordingly, the ZC_{HN} model shows only the heavy metals, while the CPK model shows only the oxygen atoms on the molecular surface. Note that we used the ZC_{HN} radii because the background of the carbonaceous substrate acts as background noise in the TEM image.

The ZC_{HN} atomic parameters reflecting nuclear charges illustrate the features of the TEM images better than the space-filling model reflecting van der Waals surfaces. Wire and ball-and-stick molecular models are not better than the space-filling model, and the atomic size is overestimated when we use ZC_{LN} radii (*SI Appendix*, Fig. S5). Outlines of the CNTs appear thick in the TEM images due to the overlapping of carbon atoms as shown in Fig. 4 using cumulene as an example, and also because the CNTs are vibrating faster than the TEM imaging rate (18, 44). Note that blur is caused by various factors in single-molecule TEM images. Although some factors such as defocus blur and energy spread of an e-beam are essentially unavoidable, a pixel blur caused by camera scintillation and a motion blur originating from a slow shutter speed will be minimized by improvement of the electron detector.

The ZC_{LN} parameter is useful for ultrathin crystalline samples as illustrated in Fig. 1*E* for UiO-66 (15), which consists of a stable network made of $[Zr_6O_4(OH)_4]$ octahedron clusters and 1,4-benzene dicarboxylic acid (BDC) ligands. The TEM image in Fig. 1*E* obtained by careful adjustment of parameters including contrast transfer function beautifully revealed the network structure, highlighted by the image of benzene rings in the BDC linker seen as benzene rings superimposed along the e-beam axis. Fig. 1*G* shows the ZC_{LN} model based on X-ray crystallographic data (45), and we see the benzene ring
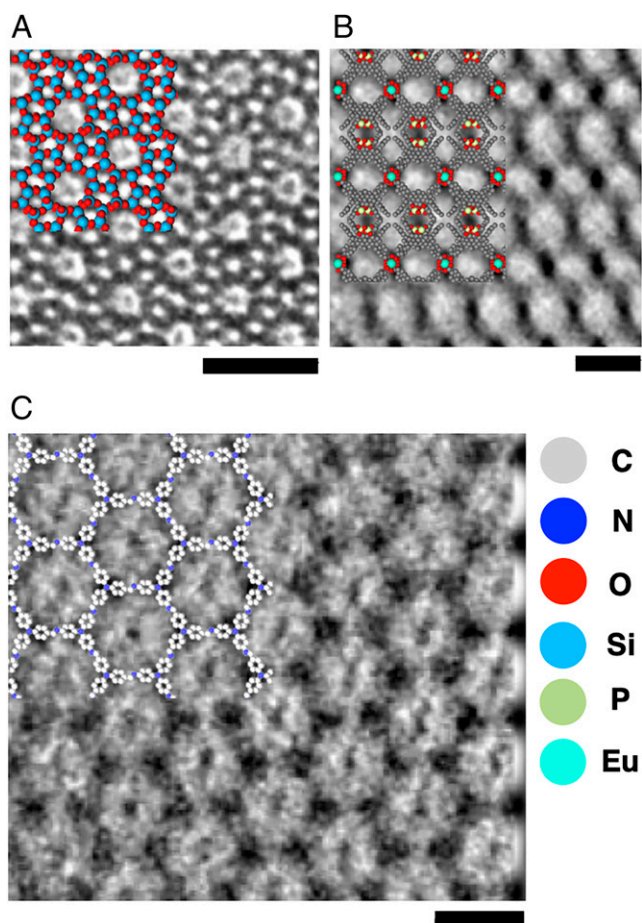

Fig. 7. TEM image and corresponding ZC_{LN} model for inorganic and organic crystals. (*A*) TEM image of ZSM-5 (Copyright 1997, American Chemical Society). (*B*) TEM images of two-dimensional metal-organic nanosheet made of 1,1′-biphenyl phosphoric acid derivative and Eu(III) (Copyright 2021, American Chemical Society). (*C*) TEM images of COF made of Tris(4-aminophenyl)amine and 1,3,5-Tris(4-formylphenyl)benzene (Copyright 2017, American Chemical Society). (Scale bars: 2 nm.)

balanced in size with the Zr atoms (sky blue). Fig. 6 *A* and *B* further illustrate application to a MOF, HKUST-1 made of dinuclear copper clusters connected by benzene-1,3,5-tricarboxylate linker molecules (15). The ZC_{LN} model made from a reported crystal structure (46) in Fig. 6*C* highlights the Cu cluster (orange) seen clearly in the TEM image.

Fig. 6*D* and *Inset* show a TEM image of a crystal of MAPbBr$_3$ (MA = methylammonium ion) seen from the [100] axis (15). Large and smaller dots corresponding to the atomic columns are arranged alternately in a grid pattern. By comparing the TEM image with the ZC_{LN} model based on a reported X-ray crystal structure (Fig. 6*E*) (47), we can assign the large dots to atomic columns consisting of alternating lead ($Z = 82$) and bromine ($Z = 35$), and the smaller dots to columns consisting of only bromine atoms. The lighter MA molecules are seen off the center of the void as smaller dots (indicated by arrows, Fig. 6*D*, *Inset*), which are reproduced well in the ZC_{LN} model (Fig. 6*E*). The simulation under the LN condition reproduces the contrast difference between the two atomic columns (Fig. 6*F*). In a simulation without shot noise the lead/bromine and the bromine columns appear similar in size (*SI Appendix*, Fig. S6), which illustrates the importance of the inclusion of shot noise in TEM simulations.

Fig. 6*G* shows a TEM image from the [100] axis of a NaCl nanocrystal in CNT (6). The alternating overlap of sodium and chloride ions in the depth direction results in an array of uniformly sized dots, reflecting the contrast of the chlorine atoms of $Z = 17$ rather than the sodium atoms ($Z = 11$) (Fig. 6*H*). This is also reproduced in the ZC_{LN} model shown in the upper right of Fig. 6 *G* and *I*, where the size of the chlorine, but not the sodium, is reflected as the size of the atomic column. The atomic size is greatly underestimated when we use ZC_{HN} radii (*SI Appendix*, Fig. S7). Fig. 7 illustrates the applicability of the ZC model to a variety of thin film materials, from inorganic to organic, as exemplified in HR-TEM images of a zeolite, ZSM-5 (Fig. 7*A*) (48), a two-dimensional coordination material (Fig. 7*B*) (49), and a covalent organic framework (COF, Fig. 7*C*) (50). We did not develop radius parameters for thick crystals, where interference among neighboring columns of atoms overwhelms the effects of interference caused by individual atoms.

In summary, we proposed ZC atomic radii for molecular modeling of AR-TEM images. Experience has taught us that heavier elements appear as both larger and denser spots than lighter elements; although, in theory, their sizes should be essentially the same. We have shown that it is the shot noise that causes the Z-dependency of the image sizes of various elements, and parameterized the ZC atomic radii by balancing the atomic number and the effects of the shot noise inherent to digital imaging. We proposed two parameter sets, ZC_{HN} and ZC_{LN}, for analysis of high-noise and low-noise AR-TEM

images, and found that the former also works well for images where the substrate provides "noise" that interferes with the signal of the specimen being studied. We expect that the method will be further modified to be better as more cases are examined. We expect that the ZC model will accelerate research on cinematic molecular science as an increasing number of chemists gain access to AR-TEM instruments, and that the present analysis on the shot noise effects and the Z dependence on the atom image size hold also in the STEM imaging if appropriate attention is paid for the variation of detectors and imaging conditions (51).

Materials and Methods

TEM Image Simulation of a Single Atom. TEM image simulation was carried out using ElBis software by parallelized computation using a graphics processing unit (29). Image simulations are generated in a 16-bit gray scale from an object exit wave function calculated with the multislice formalism (slice thickness: 0.010 nm). The atomic potential was calculated using inverse Fourier transformation from Weickenmeier–Kohl form factors (28). The details of the calculation method are described in detail in previous papers (29, 36). Computational three-dimensional atomic models of single atoms of all elements were constructed in BIOVIA Materials Studio software. Atoms are located in the same plane (e.g., the same z value) in three-dimensional space with a separation of 20 Å, where a contrast from a single atom does not interfere with that of neighboring atoms. The parameters for simulation were set to be acceleration voltage = 80 kV, spherical aberration constant C_s = –3 μm, pixel size = 0.01054 nm/pixel, defocus value = –10 nm (underfocus), which is a typical set of SMART-EM conditions at 2×10^6 magnification. TEM simulation images under a finite e-dose were generated based on the cumulative distribution of probability density (52) using an algorithm implemented in the software.

ZC_{HN} and ZC_{LN} Atomic Radii. The simulated TEM image of a single atom was processed using ImageJ 1.53c software to obtain the intensity profile. The intensity profile of the simulated atomic image was cut at two noise levels determined for the HN and LN conditions, and the length of the bottom of a triangle is defined as the ZC_{HN} and ZC_{LN} image sizes in Fig. 3*E*. The HN and LN noise levels were defined as one SD of the image intensity generated under the e-dose of 5.0×10^5 e⁻ nm⁻² s⁻¹ for HN and 4.5×10^6 e⁻ nm⁻² s⁻¹ for LN. We used these image sizes as the ZC_{HN} and ZC_{LN} atomic radii in the ZC molecular model.

Data Availability. All study data are included in the article and/or *SI Appendix*.

1. J. Brickmann, R. J. Marhöfer, T. E. Exner, M. Keil, Molecular graphics–Trends and perspectives. *J. Mol. Model.* **6**, 328–340 (2000).

2. E. Ospadov, J. Tao, V. N. Staroverov, J. P. Perdew, Visualizing atomic sizes and molecular shapes with the classical turning surface of the Kohn-Sham potential. *Proc. Natl. Acad. Sci. U.S.A.* **115**, E11578–E11585 (2018).

3. R. B. Corey, L. Pauling, Molecular models of amino acids, peptides, and proteins. *Rev. Sci. Instrum.* **24**, 621–627 (1953).

4. R. D. Shannon, Revised effective ionic radii and systematic studies of interatomic distances in halides and chalcogenides. *Acta Crystallogr. A* **32**, 751–767 (1976).

5. S. Okada *et al.*, Direct microscopic analysis of individual C$_{60}$ dimerization events: Kinetics and mechanisms. *J. Am. Chem. Soc.* **139**, 18281–18287 (2017).

6. T. Nakamuro, M. Sakakibara, H. Nada, K. Harano, E. Nakamura, Capturing the moment of emergence of crystal nucleus from disorder. *J. Am. Chem. Soc.* **143**, 1763–1767 (2021).

7. H. Hanayama, J. Yamada, I. Tomotsuka, K. Harano, E. Nakamura, Rim binding of cyclodextrins in size-sensitive guest recognition. *J. Am. Chem. Soc.* **143**, 5786–5792 (2021).

8. K. Harano, Self-assembly mechanism in nucleation processes of molecular crystalline materials. *Bull. Chem. Soc. Jpn.* **94**, 463–472 (2021).

9. M. Koshino *et al.*, Imaging of single organic molecules in motion. *Science* **316**, 853–853 (2007).

10. E. Nakamura, Atomic-resolution transmission electron microscopic movies for study of organic molecules, assemblies, and reactions: The first 10 years of development. *Acc. Chem. Res.* **50**, 1281–1292 (2017).

11. S. T. Skowron *et al.*, Chemical reactions of molecules promoted and simultaneously imaged by the electron beam in transmission electron microscopy. *Acc. Chem. Res.* **50**, 1797–1807 (2017).

12. J. Xing, L. Schweighauser, S. Okada, K. Harano, E. Nakamura, Atomistic structures and dynamics of prenucleation clusters in MOF-2 and MOF-5 syntheses. *Nat. Commun.* **10**, 3608 (2019).

13. E. J. Kirkland, "Atomic Size" in *Advanced Computing in Electron Microscopy* (Springer, ed. 2, 2010), pp. 84–85.

14. Y. Zhu *et al.*, Unravelling surface and interfacial structures of a metal-organic framework by transmission electron microscopy. *Nat. Mater.* **16**, 532–536 (2017).

15. D. Zhang *et al.*, Atomic-resolution transmission electron microscopy of electron beam-sensitive crystalline materials. *Science* **359**, 675–679 (2018).

16. D. B. Williams, C. B. Carter, *Transmission Electron Microscopy: A Textbook for Materials Science* (Springer US, New York, ed. 2, 2009).

17. K. Yamanouchi, "Scattering electrons" in *Quantum Mechanics of Molecular Structures* (Springer, 2013), pp. 197–258.
18. T. Shimizu *et al.*, Real-time video imaging of mechanical motions of a single molecular shuttle with sub-millisecond sub-angstrom precision. *Bull. Chem. Soc. Jpn.* **93**, 1079–1085 (2020).
19. L. Gross, F. Mohn, N. Moll, P. Liljeroth, G. Meyer, The chemical structure of a molecule resolved by atomic force microscopy. *Science* **325**, 1110–1114 (2009).
20. L. Talirz, P. Ruffieux, R. Fasel, On-surface synthesis of atomically precise graphene nanoribbons. *Adv. Mater.* **28**, 6222–6231 (2016).
21. D. Lungerich *et al.*, A singular molecule-to-molecule transformation on video: The bottom-up synthesis of fullerene C_{60} from truxene derivative $C_{60}H_{30}$. *ACS Nano* **15**, 12804–12814 (2021).
22. A. Markevich *et al.*, Electron beam controlled covalent attachment of small organic molecules to graphene. *Nanoscale* **8**, 2711–2719 (2016).
23. E. Nakamura, Movies of molecular motions and reactions: The single-molecule, real-time transmission electron microscope imaging technique. *Angew. Chem. Int. Ed. Engl.* **52**, 236–252 (2013).
24. R. F. Egerton, Measurement of inelastic/elastic scattering ratio for fast electrons and its use in the study of radiation damage. *Phys. Status Solidi* **37**, 663–668 (1976).
25. E. J. Kirkland, "Single atom images" in *Advanced Computing in Electron Microscopy* (Springer, ed. 2, 2010), pp. 93–95.
26. H. Koizumi, Y. Oshima, Y. Kondo, K. Takayanagi, Quantitative high-resolution microscopy on a suspended chain of gold atoms. *Ultramicroscopy* **88**, 17–24 (2001).
27. H. Rullgård, L.-G. Öfverstedt, S. Masich, B. Daneholt, O. Öktem, Simulation of transmission electron microscope images of biological specimens. *J. Microsc.* **243**, 234–256 (2011).
28. A. Weickenmeier, H. Kohl, Computation of absorptive form factors for high-energy electron diffraction. *Acta Crystallogr. A* **47**, 590–597 (1991).
29. F. Hosokawa, T. Shinkawa, Y. Arai, T. Sannomiya, Benchmark test of accelerated multi-slice simulation by GPGPU. *Ultramicroscopy* **158**, 56–64 (2015).
30. K. Cao *et al.*, Atomic mechanism of metal crystal nucleus formation in a single-walled carbon nanotube. *Nat. Chem.* **12**, 921–928 (2020).
31. A. L. Koh *et al.*, Torsional deformations in subnanometer MoS interconnecting wires. *Nano Lett.* **16**, 1210–1217 (2016).
32. A. Chuvilin *et al.*, Observations of chemical reactions at the atomic scale: Dynamics of metal-mediated fullerene coalescence and nanotube rupture. *Angew. Chem. Int. Ed. Engl.* **49**, 193–196 (2010).
33. J. M. Yuk *et al.*, High-resolution EM of colloidal nanocrystal growth using graphene liquid cells. *Science* **336**, 61–64 (2012).
34. J. C. Meyer *et al.*, Accurate measurement of electron beam induced displacement cross sections for single-layer graphene. *Phys. Rev. Lett.* **108**, 196102 (2012).
35. K. Torabi, S. Sayad, S. T. Balke, Adaptive image thresholding for real-time particle monitoring. *Int. J. Imaging Syst. Technol.* **16**, 9–14 (2006).
36. B. Gamm *et al.*, Quantitative high-resolution transmission electron microscopy of single atoms. *Microsc. Microanal.* **18**, 212–217 (2012).
37. C. L. Jia *et al.*, Determination of the 3D shape of a nanoscale crystal with atomic resolution from a single image. *Nat. Mater.* **13**, 1044–1049 (2014).
38. E. Nakamura *et al.*, Imaging of conformational changes of biotinylated triamide molecules covalently bonded to a carbon nanotube surface. *J. Am. Chem. Soc.* **130**, 7808–7809 (2008).
39. K. Harano *et al.*, Conformational analysis of single perfluoroalkyl chains by single-molecule real-time transmission electron microscopic imaging. *J. Am. Chem. Soc.* **136**, 466–473 (2014).
40. K. Harano *et al.*, Heterogeneous nucleation of organic crystals mediated by single-molecule templates. *Nat. Mater.* **11**, 877–881 (2012).
41. Y. Kratish *et al.*, Synthesis and characterization of a well-defined carbon nanohorn-supported molybdenum dioxo catalyst by SMART-EM imaging. Surface structure at the atomic level. *Bull. Chem. Soc. Jpn.* **94**, 427–432 (2021).
42. S. Hasegawa, S. Takano, K. Harano, T. Tsukuda, New magic Au_{24} cluster stabilized by PVP: Selective formation, atomic structure, and oxidation catalysis. *JACS Au* **1**, 660–668 (2021).
43. C. Bosch-Navarro *et al.*, Selective imaging of discrete polyoxometalate ions on graphene oxide under variable voltage conditions. *ACS Nano* **10**, 796–802 (2016).
44. A. W. Barnard, M. Zhang, G. S. Wiederhecker, M. Lipson, P. L. McEuen, Real-time vibrations of a carbon nanotube. *Nature* **566**, 89–93 (2019).
45. S. Øien *et al.*, Detailed structure analysis of atomic positions and defects in zirconium metal–organic frameworks. *Cryst. Growth Des.* **14**, 5370–5372 (2014).
46. A. A. Yakovenko, J. H. Reibenspies, N. Bhuvanesh, H.-C. Zhou, Generation and applications of structure envelopes for porous metal–organic frameworks. *J. Appl. Cryst.* **46**, 346–353 (2013).
47. K.-H. Wang, L.-C. Li, M. Shellaiah, K. Wen Sun, Structural and photophysical properties of methylammonium lead tribromide ($MAPbBr_3$) single crystals. *Sci. Rep.* **7**, 13643 (2017).
48. T. Ohsuna, O. Terasaki, Y. Nakagawa, S. I. Zones, K. Hiraga, Electron microscopic study of intergrowth of MFI and MEL: Crystal faults in B-MEL. *J. Phys. Chem. B* **101**, 9881–9885 (1997).
49. Y. Liu *et al.*, Single-crystalline ultrathin 2D porous nanosheets of chiral metal-organic frameworks. *J. Am. Chem. Soc.* **143**, 3509–3518 (2021).
50. Y. Peng *et al.*, Ultrathin two-dimensional covalent organic framework nanosheets: Preparation and application in highly sensitive and selective DNA detection. *J. Am. Chem. Soc.* **139**, 8698–8704 (2017).
51. S. Yamashita *et al.*, Atomic number dependence of Z contrast in scanning transmission electron microscopy. *Sci. Rep.* **8**, 12325 (2018).
52. N. Gilbert, H. O. Pollak, Amplitude distribution of shot noise. *Bell Syst. Tech. J.* **39**, 333–350 (1960).